SAND2019-5900J

Investigating Potential Kinetic Limitations to MgB_2 Hydrogenation

Y.-S. Liu[1], L.E. Klebanoff[2,*], P. Wijeratne[2], D.F. Cowgill[2], V. Stavila[2], T.W. Heo[3], S. Kang[3], A.A. Baker[3], J.R.I. Lee[3], K.G. Ray[3], J.D Sugar[2] and B.C. Wood[3]

[1]*Lawrence Berkeley National Laboratory, Berkeley, CA 94720 USA*

[2]*Sandia National Laboratories, Livermore, CA 94551-0969, USA*

[3]*Lawrence Livermore National Laboratory, Livermore, CA 94551, USA*

**Corresponding Author*

Abstract

An investigation is reported of potential kinetic limitations to MgB_2 hydrogenation. The role of H-H bond breaking, a necessary first step in the hydrogenation process, is assessed for bulk MgB_2, ball-milled MgB_2, as well as MgB_2 mixed with Pd, Fe and Ti additives. The Pd and Fe additives in the MgB_2 material exist as dispersed metallic particles in the size range ~ 2 – 35 nm diameter. In contrast, TiF_3 reacts with MgB_2 to form Ti metal, elemental B and MgF_2, with the Ti and the MgF_2 phases proximate to each other and distributed throughout the MgB_2 base solid. The TiF_3/MgB_2 system was examined theoretically with reaction thermodynamics and phase nucleation kinetic calculations to better understand the production of Ti metal when TiB_2 is thermodynamically favored. Sieverts studies of hydrogenation kinetics are reported and compared to the rate of H-H bond breaking as measured by H-D exchange studies. The results show that H-H bond dissociation does not limit the rate of hydrogenation of MgB_2 because H-H bond cleavage occurs rapidly compared to the initial MgB_2 hydrogenation. The results also show that surface diffusion of hydrogen atoms cannot be a limiting factor for MgB_2 hydrogenation. Instead, it is speculated that it is the intrinsic stability of the B-B extended hexagonal ring structure in MgB_2 that hinders the hydrogenation of this material. This supposition is supported by B K-edge x-ray absorption measurements of the materials, which showed spectroscopically that the B-B ring was intact in these material systems.

Introduction

Hydrogen fuel cells are finding deeper and wider use in our technical society to provide zero-emissions electrical power. The advantages of fuel cells versus diesel engines are higher thermal efficiency (especially at partial load), dramatically lower noise, reduced maintenance and associated costs, and emissions-free operation at the point of use [1]. In addition, the modularity of fuel cells allows for power architectures that can be more efficiently matched to the power utilization profile of the particular application. Most major auto manufacturers have designs for light-duty fuel-cell vehicles, with Toyota, Honda and Hyundai already making these vehicles available to the public for sale or lease. Beyond light-duty vehicles, fuel-cell versions of buses

have been in service already for many years [2], fuel-cell construction lighting equipment has been demonstrated [3], fuel-cell forklifts are now in routine use by the thousands [4] and the first light rail systems operated by hydrogen fuel cells are now operational [5]. In the last few years the feasibility of using hydrogen fuel cells to replace marine diesel engines in maritime applications has been shown, for example in high-speed ferries [6] and coastal research vessels [7]. A hydrogen fuel-cell ferry is currently under construction for use on the San Francisco Bay beginning in the Fall of 2019 [8]. Fuel-cell vessels represent a high-impact use of hydrogen. A typical high-speed ferry would use the equivalent amount of hydrogen as ~2000 light duty vehicles. Still, the sheer number of light-duty vehicles (~ 1 billion worldwide) makes hydrogen fuel-cell cars the largest technical driver of hydrogen fuel-cell technology development.

The current light-duty fuel-cell cars store hydrogen as a high-pressure gas, with the hydrogen stored at either 350 bar or 700 bar in composite hydrogen tanks. These tanks provide the required hydrogen gravimetric and volumetric storage densities for the rollout of fuel-cell vehicles with acceptable range. However, if the hydrogen storage densities could be improved, an even greater range for fuel-cell cars could be realized. Liquid hydrogen (LH_2) can provide higher hydrogen storage densities. However, the relatively small amount of hydrogen needed for light-duty fuel-cell vehicles, ~ 5 kg, makes LH_2 storage impractical because of the high heat leak rate (and subsequent boil-off) associated with small cryogenic tanks. Liquid hydrogen is better suited for applications requiring large quantities of stored hydrogen, for example in watercraft and in aerospace applications.

It has been recognized for many years that solid-state storage of hydrogen has the potential to improve hydrogen storage efficiency beyond that achieved with 700 bar tanks. For example, while the volumetric storage density of 700 bar hydrogen gas is 40 g/L, the volumetric hydrogen storage density of aluminum hydride (AlH_3) is 149 g/L, even higher than that of LH_2 (71 g/L). The challenge for solid-state hydrogen storage materials is that they must satisfy at least 4 major criteria: 1) they must release hydrogen quickly enough when demanded by the fuel cell (~ 1.6 g/s for a 80 kW fuel cell); 2) the hydrogen must be very pure (as specified by the SAE J2719 standard [9]) to avoid poisoning the fuel-cell catalyst; 3) the material must release hydrogen with very little input energy (have the right thermodynamics) and 4) the material must be able to be refueled (rehydrogenated) in 3-5 minutes with gaseous hydrogen [10]. All known hydrogen storage materials fail to meet at least one of these requirements for the light-duty fuel-cell vehicle application. For example, AlH_3, which is an exemplary hydrogen storage material in many respects, forms Al when its hydrogen is released. However, it is essentially impossible, in the context of a hydrogen refueling station, for Al to be rehydrogenated back to AlH_3 [11]. It has become clear to the hydrogen storage community that addressing the technical shortcomings of current hydrogen storage materials requires a full understanding of the fundamental chemical and physical limitations to performance. With this understanding, overcoming such shortcomings will enable these materials to be used to store hydrogen for light-duty fuel-cell vehicles and other applications.

Magnesium borohydride, $Mg(BH_4)_2$, is a material with a very high hydrogen capacity of 14.9 weight percent which can be achieved by the following overall reaction: $Mg(BH_4)_2 = 4H_2 + MgB_2$. Much work has been devoted to understanding how this material releases hydrogen, as reviewed by Zavorotynska et al. [12]. In comparison, there have been relatively few studies aimed at understanding how MgB_2 can be fully hydrogenated to form $Mg(BH_4)_2$. The status of the rehydrogenation has been reviewed by Ray et al. [13]. Although possible, the complete conversion of MgB_2 to $Mg(BH_4)_2$ requires excessively high pressures (950 bar) and temperatures (400 °C) and requires too much time (a day) for practical applications [14]. Ray et al. [13] investigated the initial hydrogenation of the material both experimentally and theoretically to understand the mechanism by which hydrogen first absorbs to MgB_2. However, the fundamental reasons why MgB_2 is so slow to rehydrogenate are not understood. Given the dramatic improvement needed in the rehydrogenation kinetics of the $Mg(BH_4)_2/MgB_2$ system, we embarked on a study to examine two potential limitations to the rehydrogenation kinetics: H-H bond breaking and surface diffusion of H atoms.

Our primary objective is to assess if H-H bond breaking—a necessary first step in the hydrogenation of MgB_2 by H_2 gas—is a rate-limiting reaction step. Our approach is to introduce additives into MgB_2 that are known to independently dissociate H_2 and probe whether or not their introduction increases the rate of the initial MgB_2 hydrogenation observed at the relatively modest applied hydrogen pressures of ~ 130 bar used in a Sieverts apparatus. For this study we have chosen three additives: Pd metal, Fe metal, and TiF_3. Pd metal and Fe metal are elements that have demonstrated their ability to catalytically break the H-H bond in diverse morphological forms. Pd metal dissociates hydrogen at its (100), (110) and (111) surfaces [15-17]. The (100), (110) and (111) surfaces of Fe also readily dissociate the H-H bond [18-20]. Hydrogen can also be dissociated by thin films of both Pd [21,22] and Fe [22,23], as well as by dopants of these metals [24-26]. TiF_3 is in a different class, not being an elemental metal, but nonetheless has demonstrated positive influence on the hydrogen storage kinetics of some systems as reviewed by Kang et al. [27]. Such a promotion must involve chemical transformation of TiF_3, since it has been shown that TiF_3 is completely inert to hydrogen under the relevant conditions of hydrogen pressure and temperature [27]. We shall see that Ti metal is produced when TiF_3 is combined with MgB_2. Ti metal is known to dissociate hydrogen as well, whether in the form of a single-crystal surface [28,29], as a film [22] or as a dopant [26, 30].

For these additives to promote H-H bond breaking, they should be introduced into the MgB_2 solid preferably without oxidation or other contamination, since their oxides do not dissociate hydrogen [31,33]. Also, their structural and chemical state in the MgB_2 matrix must be understood. Toward these ends, we have conducted extensive characterization of the materials produced by ball-milling the additives Pd, Fe and TiF_3 with MgB_2, including powder x-ray diffraction (XRD), Fourier Transform Infra-red (FTIR) spectroscopy, x-ray absorption spectroscopy (XAS) and transmission electron microscopy (TEM) combined with energy-dispersive x-ray spectroscopy (EDS). With the structural/chemical aspects understood, the

additive/MgB_2 materials are then be exposed to hydrogen in a Sieverts apparatus in order to assess the effect of the additive on the kinetics of MgB_2 hydrogenation. To independently confirm the promotion of H-H bond breaking in these materials, we use a novel H-D exchange study approach that we recently introduced into hydrogen storage work to confirm the chemical inertness of TiF_3 and $TiCl_3$ additives when exposed to hydrogen [27]. While H-D exchange studies have been used before in studies of dehydrogenation [34-36], its use for hydrogenation studies is relatively new. We supplement these experimental studies with theoretical work clarifying the physical phenomena involved.

Experimental and Theoretical Methods

All sample handling and preparation was conducted in an Ar-filled glove-box equipped with a recirculation system that keeps H_2O and O_2 concentrations below 0.1 ppm. Commercial grade MgB_2 and additives where purchased from commercial sources as described in the Supporting Information (SI).

The ball-milled materials were produced by loading tungsten carbide (WC) mill pots (SPEX Sample Prep, No. 8004) with the appropriate commercially available chemicals and milling with two 7/16" diameter WC balls (SPEX Sample Prep, No. 8004A) in argon for the times indicated. Viton gaskets (SPEX Sample Prep, No. 39322) were used for the milling vials due to their superior sealing ability and chemical resistance. Milling was conducted using a SPEX Sample Prep 8000M high-energy mixer mill.

A variety of substances used in the study were either prepared or used directly from commercial sources without further purification. These include: commercial MgB_2; MgB_2 ball-milled 2 hours and MgB_2 ball-milled 1 hour. In addition, a series of additive/MgB_2 samples were made including:

1. MgB_2 + 4.88% Fe; where Fe powder was added to the commercial MgB_2 powder and milled for 2 hours. The mole fraction of Fe to MgB_2 was 0.0488, or 4.88% Fe.

2. MgB_2 + 4.97% Pd; Pd powder was added to the commercial MgB_2 powder and milled for 2 hours. The mole fraction of Pd to MgB_2 (moles Pd/moles MgB_2) was 0.0497, or 4.97% Pd.

3. MgB_2 + 4.46% TiF_3; where TiF_3 powder was added to the commercial MgB_2 powder and milled for 2 hours. The mole fraction of TiF_3 to MgB_2 was 0.0446, or 4.46% TiF_3

More details of the synthesis of these materials can be found in the SI.

An extensive series of characterization studies were performed to check for sample integrity, potential contamination during handling and ball-mill processing and for possible reaction

products. X-ray diffraction was used to investigate crystal structures and to check for crystalline contamination or reaction products. In addition, FTIR spectroscopy was used to check for amorphous contamination and reaction products that would not be detected by XRD. Element-specific core-level XAS was used to evaluate the local electronic structure at the B and additive sites. The details of the many materials characterization studies are provided in the SI.

XRD measurements were made using a PANalytical Empyrean diffractometer. FTIR spectra were collected in attenuated total internal reflectance (ATR) mode using a compact Cary 630 spectrometer located within the Ar glovebox. The ATR crystal was diamond, and all FTIR spectra are reported as absorbance measurements. XAS measurements at the Ti $L_{2,3}$ edge, the F K edge, the Fe $L_{2,3}$ edge, the Pd $M_{4,5}$ edge and at the B K edge were performed at beamlines (BLs) 6.3.1.2 and 8.0.1.1 of the Advanced Light Source (ALS), Lawrence Berkeley National Laboratory (LBNL), and at the Resonant Elastic and Inelastic X-ray Scattering (REIXS) beamline (BL10ID-2) of the Canadian Light Source (CLS). All experimental samples and standards were transferred to the experimental endstations of BLs 6.3.1.2 and 8.0.1.1 under argon using a vacuum suitcase to prevent exposure to atmospheric oxygen and water. Samples measured at the CLS were transferred using an Ar-purged glove bag with a partial pressure of < 25 ppm water. XAS data were simultaneously recorded in two modes: total electron yield (TEY) [37] (via measurement of the drainage current to the experiment sample) and total fluorescence yield (TFY) [38] (using a channeltron electron multiplier). All XAS spectra presented are normalized to the incident x-ray flux, I_0, which was measured concurrently as a drainage current from an upstream gold mesh and scaled to the magnitude of the absorption edge step. The depth sensitivities of the TEY and TFY XAS data are discussed in the SI for the various core-level absorption edges employed in this study.

TEM measurements were made using a probe-corrected FEI Titan Themis Z instrument operated at 300 kV with EDS data collected using a large-solid-angle Super X detector. Samples undergoing TEM analysis were briefly exposed to air prior to introduction to the TEM apparatus. This was deemed acceptable because we were primarily interested in using TEM to reveal the location of elemental constituents rather than their chemical state, which was studied with other techniques.

The capacity for the materials under study to dissociate H_2 was assessed using a Sandia-built "in-house" apparatus that provides exposure to calibrated mixtures of H_2 and D_2, at ~ 10 Torr pressure and for temperatures from 22 °C to 300 °C. The breaking of H-H and D-D bonds were monitored by measuring the partial pressure of HD generated as a function of time with a residual gas analyzer (RGA). Figure S1 in the SI shows a diagram of the H_2/D_2 isotope exchange experimental setup. The method of H-D exchange measurement is described in the SI.

The samples were exposed to hydrogen in a Sieverts apparatus to assess the rate of hydrogen uptake when the materials were exposed to hydrogen. The Sieverts measurements employed a PCTPro 2000 apparatus from Setarem. The samples were loaded inside a sample holder inside the

Ar glove box, with a thermocouple placed in the center of the sample holder for accurate temperature measurements during the hydrogen absorption and desorption experiments. Pressure changes during the hydrogenation of the samples were quantified with calibrated pressure transducers. Baseline measurements without any sample and with stainless steel spacers in the reactor were performed for normalization and background subtraction. Hydrogen capacity data are presented as weight percent of H absorbed with respect to the total sample weight: wt.% absorbed = [mass H absorbed]/[(mass H absorbed + mass MgB_2 original sample) x 100.

To understand better the chemical reaction that was observed between MgB_2 and TiF_3, the reaction thermodynamics and nucleation kinetics for this system were computed by combining the NIST-JANAF thermochemical database [39], density functional theory (DFT) total energy calculations and classical nucleation theory [40]. Bulk and surface energies of involved phases were obtained from the NIST-JANAF database or literatures if available, and otherwise computed within DFT using Vienna *ab initio* Simulation Package [41]. More computational details are described in the SI.

Results

Materials Characterization

To fully understand the effect of the additives on the hydrogenation of MgB_2, the chemical and structural nature of these additive/MgB_2 systems requires detailed characterization. The SI provides full details of the XRD, FTIR, XAS and TEM studies of these systems. The essential results are summarized here.

MgB_2 + 4.88% Mole Fraction Fe

We refer to the sample made by ball milling together for 2 hours in argon a mixture of MgB_2 with 4.88% mole fraction of Fe metal powder as [MgB_2 + 4.88 % Fe]. The starting Fe powder was characterized by XRD and FTIR to check for iron oxide contamination. The XRD results indicated no evidence for crystalline oxide contamination. However, FTIR indicated trace Fe_3O_4 oxidation. For the [MgB_2 + 4.88 % Fe] material, neither XRD nor FTIR showed any evidence for MgO or B-O species (e.g. B_2O_3) which could have been produced by an air leak in the WC milling vial. No evidence was found for FeB formation, which could be formed if the Fe metal reacted with MgB_2. These results are presented in the SI.

An XRD pattern for [MgB_2 + 4.88 % Fe] is shown in Figure 1, where it is compared to patterns for MgB_2 without additive and Fe metal. The MgB_2 XRD (101) peak for [MgB_2 + 4.88 % Fe] at 42.50 degrees is shifted slightly (by 0.1 degrees 2θ) to larger angle compared to MgB_2 that was milled for the same amount of time only with no Fe added. The FWHM broadenings of the MgB_2 peaks are similar, with the FWHM value indicating a dimension for the diffractive zone of

~ 8 nm as inferred from Scherrer's Equation [42] (see the SI). The (110) peak positions for the Fe powder, and the Fe in [MgB_2 + 4.88 % Fe] are identical at 44.67 degrees 2θ. This indicates that the Fe particulates have unaltered interplanar spacings in the MgB_2 mixture, suggesting that the Fe has not reacted with MgB_2. The Fe crystallite size in the mixture (~ 23 nm) is smaller than in the original Fe powder (~ 44 nm) due to ball-milling.

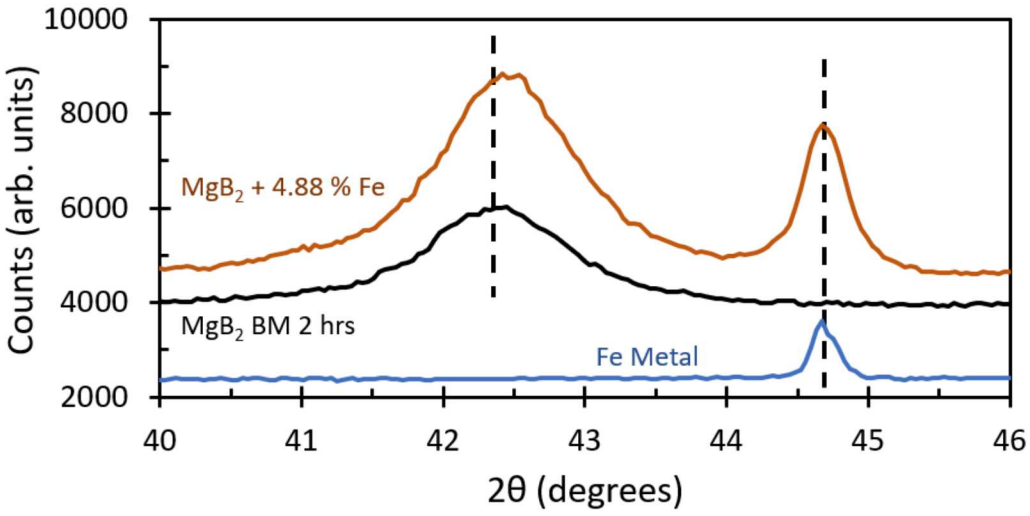

Figure 1: XRD patterns for [MgB_2 + 4.88 % Fe], MgB_2 ball-milled for 2 hours and Fe metal powder.

X-ray absorption spectroscopy at the Fe $L_{2,3}$ edge was used to probe the reactivity and oxidation of the Fe additive in [MgB_2 + 4.88 % Fe]. Figures 2(a) and 2(b) show the Fe $L_{2,3}$ edge XAS data collected in TFY and TEY modes, respectively for [MgB_2 + 4.88 % Fe], the starting Fe powder and several relevant standards. The depth sensitivities of the Fe $L_{2,3}$-edge TFY and TEY spectra are estimated to be ~ 1600 nm and ~23 nm, respectively. We define the depth sensitivity as including depths that contribute greater than or equal to 10% of the signal associated with the surface layer. The depth dependence of all of the XAS spectra is given in the SI.

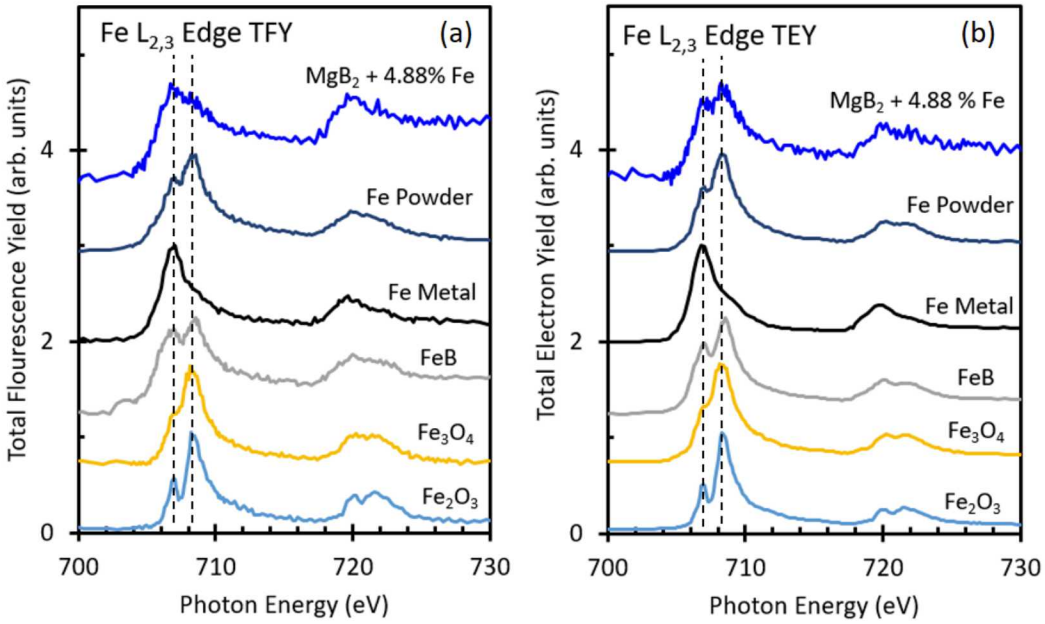

Figure 2: (a) Fe $L_{2,3}$ edge x-ray absorption collected in TFY mode; (b) Fe $L_{2,3}$ edge x-ray absorption collected in TEY mode. The vertical dotted lines are aligned on the largest peaks of Fe metal and Fe_3O_4 and serve as a guide for the eye.

The TFY and TEY data illustrate that the starting Fe powder most closely resembles the XAS spectrum of Fe_3O_4 standard powder. This is confirmed by FTIR results in the SI, which detected Fe_3O_4 contamination at the surface of the starting Fe metal powder. The XAS TFY depth sensitivity indicates the oxide is present in the first ~ 1600 nm of the Fe powder. The XAS from the [MgB_2 + 4.88 % Fe] sample displays a greater prominence at 707 eV, which is consistent with the presence of unoxidized Fe. This behavior is seen most notably in the TFY data but is also apparent in the TEY data. This greater prominence of metallic Fe is attributed to ball-milling of the material, which can break up the near-surface oxide layers of the Fe metal powder, exposing clean metal underneath.

It is unclear from the Fe $L_{2,3}$-edge XAS data alone if Fe has reacted with B to form FeB because of the similarity of the FeB and Fe_3O_4 XAS spectra. However, the entirety of the characterization data (XRD, FTIR, XAS) presented in the SI are consistent with the Fe additive in [MgB_2 + 4.88 % Fe] existing as Fe metal with near-surface Fe_3O_4 contamination.

The morphology and elemental composition of [MgB_2 + 4.88 % Fe] was examined with TEM in combination with EDS. Characteristic TEM images are presented in Figure 3, with more results provided in the SI.

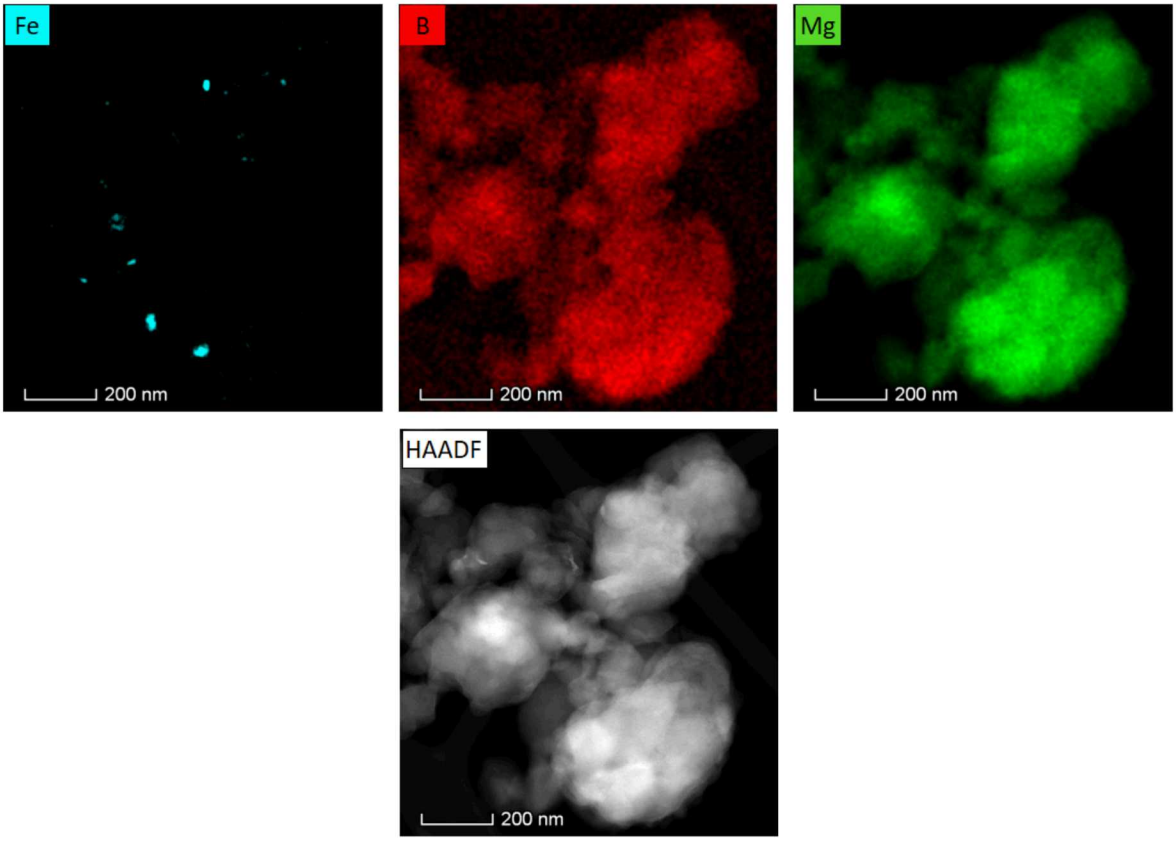

Figure 3: TEM investigation of [MgB_2 + 4.88 % Fe], giving the particle size, morphology and the elemental contributions and distributions as determined by EDS. (Top): EDS results for Fe, B and Mg; (Bottom): Bright-field (HAADF) image.

The bright-field image shows larger (~ 300 nm) agglomerations of smaller MgB_2 particles. The elemental maps show that the particles consist of Mg and B, consistent with MgB_2. The MgB_2 particles are decorated with small Fe particles, with a range of particle sizes from ~ 12 – 40 nm in diameter. This particle size is in good accord with the estimate of the average Fe crystallite size of ~ 23 nm made from XRD analysis of the Fe (110) peak in Figure 1. A few larger flakes of Fe in the range 20 – 150 nm in size were also observed. There no evidence for atomic-scale dispersal of the Fe additive. Rather, it exists as integral particles, whose d-spacing is identical to the original starting Fe powder, as revealed by the XRD data of Figure 1 and discussed in more detail in the SI.

MgB_2 + 4.97% Mole Fraction Pd

We refer to the sample made by ball milling together for 2 hours in argon a mixture of MgB_2 with 4.97% mole fraction of Pd metal powder as [MgB_2 + 4.97 % Pd]. The starting Pd metal powder, consisting of micron-sized particulates, was synthesized as described in the SI. XRD

and FTIR measurements of [MgB_2 + 4.97 % Pd] showed no evidence for oxidation of the sample (e.g. MgO, B_2O_3, PdO). There is XRD evidence for a small amount of Pd_2B, as described in the SI. An XRD pattern of [MgB_2 + 4.97 % Pd] is shown in Figure 4 and compared to patterns for MgB_2 without additive and Pd metal.

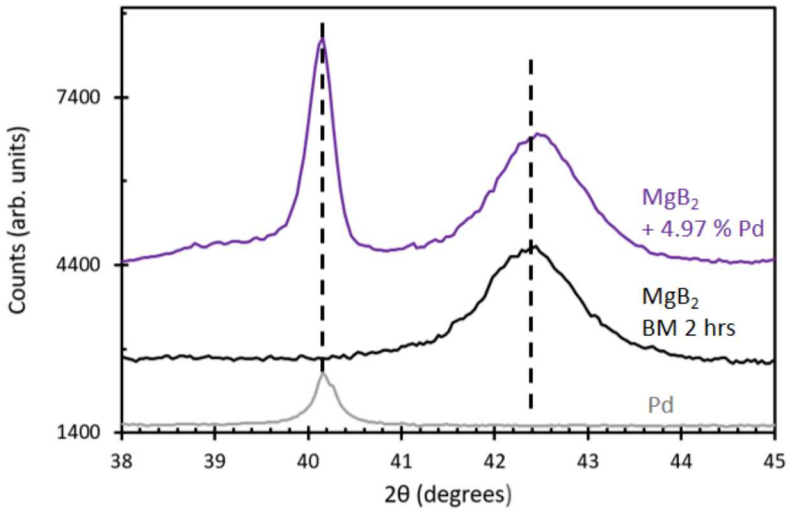

Figure 4: XRD patterns for [MgB_2 + 4.97 % Pd], MgB_2 ball-milled for 2 hours and Pd metal powder.

The MgB_2 (101) XRD peak for [MgB_2 + 4.97 % Pd] at 43.53 degrees is shifted 0.13 degrees to larger 2θ angle compared to MgB_2 that was milled for the same amount of time, only with no Pd added. The FWHM broadenings of the MgB_2 peaks are similar, indicating crystallite sizes of ~ 8 nm. The SI gives more information regarding the line positions, peak broadenings and the particle size (inferred from Scherrer's Equation) for the MgB_2 (101) and Pd (111) XRD peaks.

The (111) peak positions for Pd metal powder, and the Pd in [MgB_2 + 4.97 % Pd] are the same to within the 0.05 degrees 2θ reproducibility of the measurement. Thus, the Pd particulates in [MgB_2 + 4.97 % Pd] have the same d-spacings as bulk Pd powder, suggesting that the crystalline Pd has not reacted with MgB_2, although the possibility of small amounts of Pd_2B formation was suggested previously by XRD data shown in the SI. The Pd crystallite size in the ball-milled mixture is ~27 nm, lower than that found for the bulk Pd powder (~33 nm).

We attempted to characterize the [MgB_2 + 4.97 % Pd] material with XAS at the Pd $M_{4,5}$ edge, but were unable to observe this Pd XAS signal due to the combination of low Pd concentration and small Pd $M_{4,5}$ edge x-ray absorption cross section.

TEM was used to examine the morphological and elemental composition of [MgB_2 + 4.97 % Pd]. A series of TEM images is shown in Figures 5, with more results displayed in the SI.

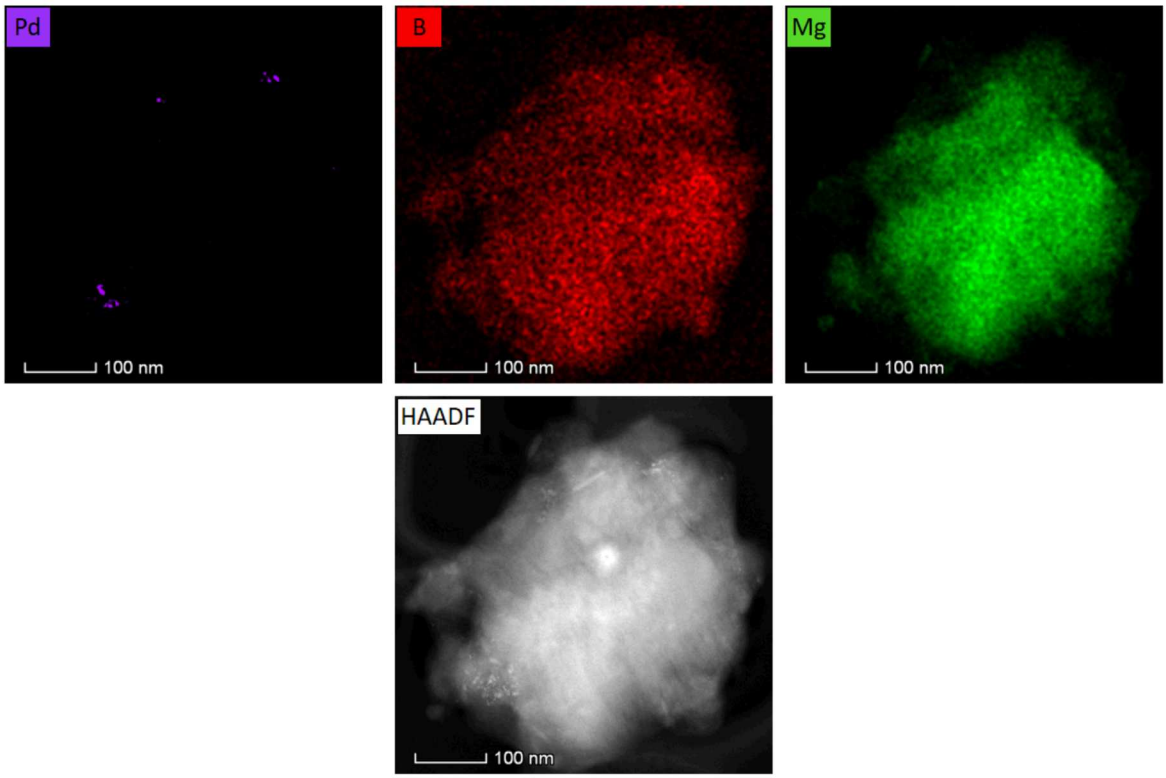

Figure 5: TEM investigation of [MgB_2 + 4.97 % Pd], giving the particle size, morphology and the elemental contributions and distributions as determined by EDS. (Top): EDS results for Pd, B and Mg; (Bottom): Bright-field (HAADF) image.

The bright-field image shows larger (~ 300 nm) agglomerations of smaller MgB_2 particles. The EDS maps show that the particles consist of Mg and B, consistent with MgB_2. The Pd in the material exists as discrete Pd particles with ~ 5 – 12 nm diameters, which is smaller than that inferred from XRD of 27 nm (see the SI). A few larger flakes of Pd were observed with ~ 50 nm size which could account for the discrepancy. The XRD of this sample showed the Pd additive has a d-spacing identical to that of bulk Pd. Analysis of the TEM images indicated no evidence for an atomically dispersed Pd component in the MgB_2 matrix.

MgB_2 + 4.46% Mole Fraction TiF_3

Characterization measurements were performed for the mixture of MgB_2 with 4.46% mole fraction of TiF_3 powder, milled for 2 hours in an Ar-filled milling vial. We refer to this sample as [MgB_2 + 4.46 % TiF_3].

As described in the SI, XRD and FTIR was used to check the starting TiF_3 powder for oxidation to TiO_2 and for other contaminants. While neither crystalline nor amorphous TiO_2 could be observed, we did find evidence for trace water contamination via the O-H stretch in the FTIR.

TiF_3 was found to be stable under ball-milling, with broadened diffraction peaks indicative of a smaller crystallite size as the TiF_3 material is ball-milled. These results are consistent with previously reported XRD studies of TiF_3 additive [27].

XRD and FTIR was used to check [MgB_2 + 4.46 % TiF_3] for contamination. No evidence was found for contamination of [MgB_2 + 4.46 % TiF_3] by crystalline oxides of B, Mg or Ti. In contrast with the starting TiF_3 material, no evidence for trace water could be seen in [MgB_2 + 4.46 % TiF_3] by FTIR. It is likely that the adventious water desorbed from the TiF_3 material during ball milling. There also was no evidence found for reaction of the Ti additive with MgB_2 to form TiB_2 as a possible reaction product.

XRD studies of [MgB_2 + 4.46 % TiF_3] presented in the SI show the complete disappearance of the crystalline TiF_3 diffraction peaks. Since our characterization work showed that TiF_3 is stable with ball-milling, the disappearance of TiF_3 in the XRD represents chemical reaction with MgB_2. However, there was no sign of a crystalline chemical product of such a reaction in the XRD data for [MgB_2 + 4.46 % TiF_3], shown in the SI. For example, one possible reaction product is the formation of MgF_2. However, there is no evidence from the XRD data for the formation of crystalline MgF_2.

FTIR was used to examine the [MgB_2 + 4.46 % TiF_3] material for any spectral signatures of amorphous products not seen in XRD. The results are shown in Figure 6.

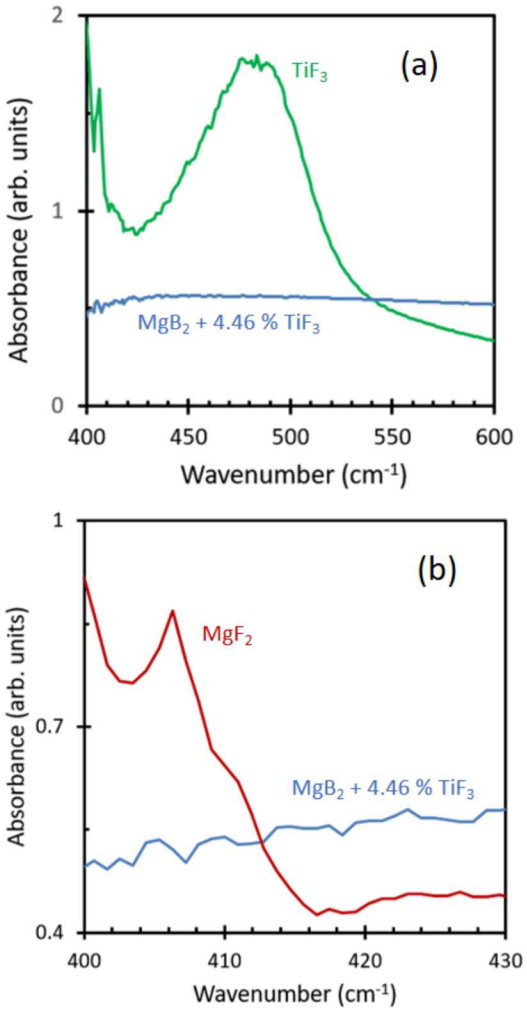

Figure 6: (a) FTIR spectra of the starting TiF_3 powder and the [MgB_2 + 4.46 % TiF_3] material, emphasizing the region of Ti-F stretch; (b) FTIR spectra of [MgB_2 + 4.46 % TiF_3] and MgF_2 standard powder.

Figure 6(a) shows that the intense Ti-F stretch of TiF_3 completely disappears upon formation of the [MgB_2 + 4.46 % TiF_3] material. From a sensitivity analysis, we estimate that we could detect as little as 1 mole percent of TiF_3 in the [MgB_2 + 4.46 % TiF_3] material via the intense Ti-F stretch, if TiF_3 existed in the sample.

Figure 6(b) compares the FTIR spectra of MgF_2 standard powder with [MgB_2 + 4.46 % TiF_3]. No evidence is found for amorphous MgF_2, however our sensitivity to MgF_2 is poor because it possesses a weaker vibrational signature than TiF_3. We estimate that the entire 4.46% mole fraction of TiF_3 could have converted to MgF_2 when ball milled with MgB_2 and it would be difficult to detect it by FTIR. Thus, both FTIR and XRD confirm the reaction of TiF_3 with MgB_2, but neither technique can identify the reaction product formed.

To identify the reaction product, XAS measurements were performed for [MgB_2 + 4.46 % TiF_3], the results of which are presented in Figures 7 and Figure 8 for the F K-edge and Ti $L_{2,3}$-edge, respectively.

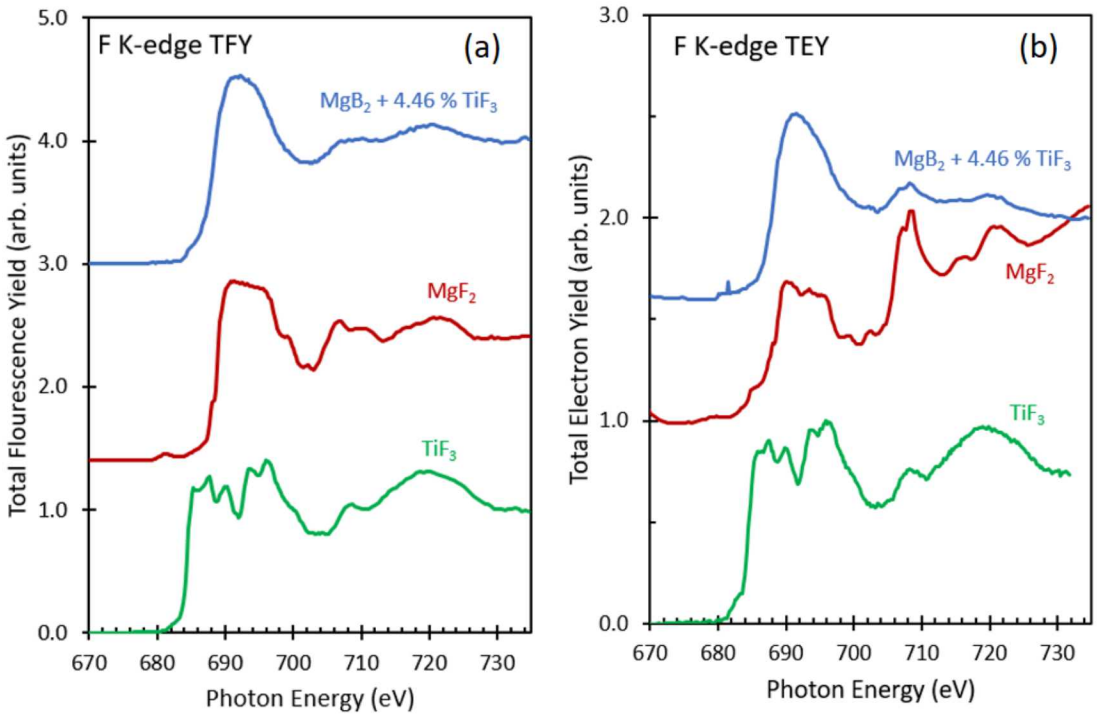

Figure 7: (a) F K-edge TFY and (b) F K-edge TEY spectra for TiF_3, MgF_2 standard powder and [MgB_2 + 4.46 % TiF_3].

The depth sensitivities of the F K-edge TFY and TEY spectra are estimated to be ~ 1500 nm and ~ 20 nm, respectively (see the SI), while those for the Ti $L_{2,3}$-edge TFY and TEY spectra are estimated to be ~500 nm and ~10 nm, respectively. The F K-edge data show that the character of F in [MgB_2 + 4.46 % TiF_3] no longer resembles TiF_3, confirming the complete reaction of TiF_3 with MgB_2 found from the FTIR and XRD data. The F K-edge for [MgB_2 + 4.46 % TiF_3] most resembles that observed for MgF_2. We therefore conclude that MgB_2 and TiF_3 react to form MgF_2 when ball-milled together. This chemical transformation and production of MgF_2 happens at all depth scales, since the TFY and TEY data in Figure 7 for [MgB_2 + 4.46 % TiF_3] are so similar.

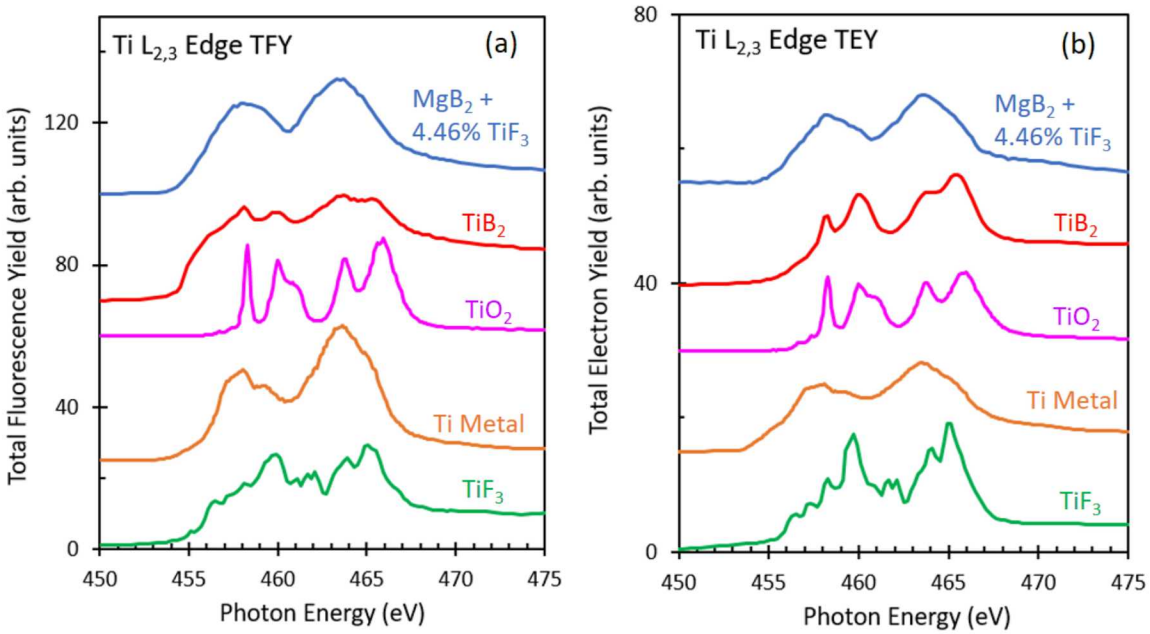

Figure 8: Ti $L_{2,3}$-edge XAS spectra recorded via the (a) TFY and (b) TEY detection modes for TiF_3, Ti metal scraped clean by surface abrasion in the glove-box immediately prior to measurement, TiO_2 standard powder, TiB_2 standard powder and [MgB_2 + 4.46 % TiF_3].

Figure 8 shows that Ti $L_{2,3}$-edge XAS data of [MgB_2 + 4.46 % TiF_3] does not resemble that acquired from TiF_3, confirming reaction between TiF_3 and MgB_2. Furthermore, the spectrum for [MgB_2 + 4.46 % TiF_3] does not resemble TiO_2, or TiB_2, which supports the conclusions drawn from XRD and FTIR measurements that TiO_2 does not exist in the sample from oxidation, and that TiB_2 is not produced by the chemical reaction. Care was taken in confirming the high-purity of the TiB_2 standard powder used in making this spectral assessment (see the SI). The Ti $L_{2,3}$-edge XAS data from [MgB_2 + 4.46 % TiF_3] most closely resembles that of clean Ti metal. Thus, we conclude that in addition to the production of MgF_2, the ball milling of TiF_3 and MgB_2 produces Ti metal, or at least dispersed Ti with zero oxidation state.

TEM was used to examine the morphological and elemental composition of [MgB_2 + 4.46 % TiF_3]. Typical results are show in Figure 9, with additional TEM data provided in the SI.

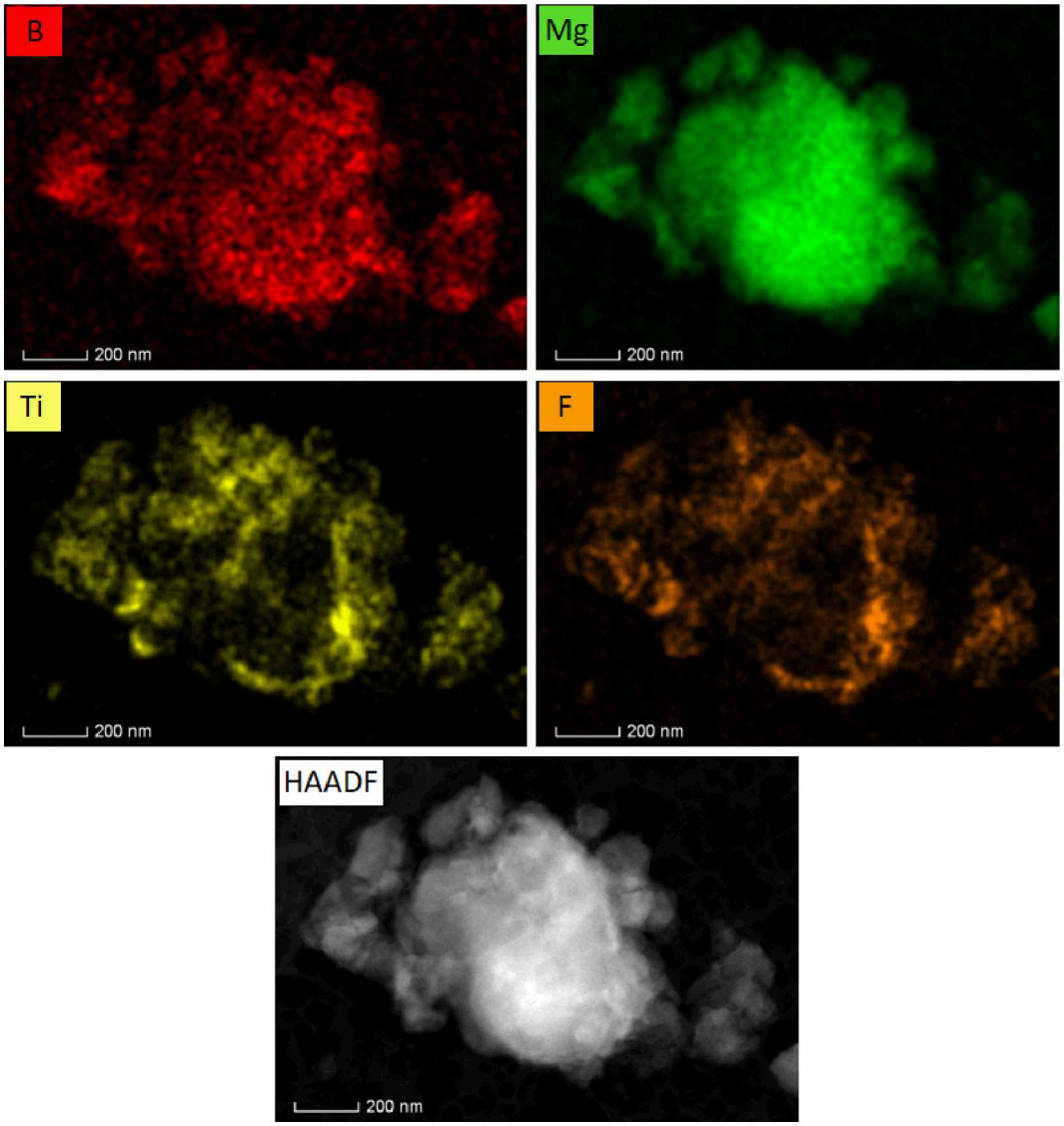

Figure 9: TEM investigation of [MgB_2 + 4.46 % TiF_3], giving the particle size, morphology and the elemental contributions and distributions as determined by EDS. (Top): EDS results for B and Mg; (Middle): EDS results for Ti and F; (Bottom): Bright-field (HAADF) image.

The bright-field image of [MgB_2 + 4.46 % TiF_3] shows larger (~ 300 nm) agglomerations of smaller MgB_2 particles. The EDS maps show that the particles are consistent with MgB_2. There is no evidence for discrete additive particles in [MgB_2 + 4.46 % TiF_3], of either Ti metal or MgF_2. Rather, the Ti and the F seem so be smeared out within the MgB_2 base solid. The dispersion is not complete, as the F is generally spatially associated with the Ti, indicating that the reaction remains local, preventing Ti^0 and MgF_2 from diffusing completely uniformly throughout the MgB_2 material. This is most clearly seen in the Ti and F maps of Figure 9, which show widespread but not completely homogeneous Ti and F distribution on the MgB_2 particles. When analyzed in conjunction with the XAS results, these TEM findings are consistent with the

formation of films of Ti metal and MgF_2 from local chemical reaction between TiF_3 and MgB_2, spread across the MgB_2 solid.

There have been no prior studies of the reaction of TiF_3 with MgB_2 in the inorganic chemistry literature. However, the reaction between $TiCl_3$ and MgB_2 has been investigated [43]. When $TiCl_3$ and MgB_2 are heated to 850 °C for 18 hours, TiB_2 and $MgCl_2$ are formed via the reaction $TiCl_3 + 3/2MgB_2 \rightarrow TiB_2 + 3/2MgCl_2 + B$. The formation of the thermodynamically stable $MgCl_2$ product drives the reaction [43]. It is interesting to note that when the reaction temperature is lowered to 550 °C, Ti metal is reported to exist along with TiB_2 [43].

On the other hand, our analysis indicates that the reaction occurring between TiF_3 and MgB_2 in our study corresponds to $TiF_3 + 3/2MgB_2 \rightarrow Ti + 3B + 3/2MgF_2$. This is particularly surprising since MgF_2 has a more negative ΔH_f (-1124 kJ/mole) than $MgCl_2$ (-641 kJ/mole), meaning the reaction should be even more thermodynamically driven by the magnesium fluoride product. As a result, we conclude that the product Ti metal must be *kinetically* favored over TiB_2, and that the thermodynamically stable product is inaccessible because the ball milling is taking place at nominally room temperature. We point out that our proposed reaction pathway requires that 3 moles of elemental B are produced for every mole of Ti metal produced. We propose that elemental B is present, but it must be produced as an undetected amorphous phase. This conclusion derives from the fact there was no evidence for crystalline B in the XRD of [MgB_2 + 4.46 % TiF_3]. Note that elemental B is not detectable by FTIR, and XAS spectroscopy cannot readily distinguish elemental B from MgB_2, so these probes cannot act as secondary confirmation.

Theoretical Results

To better understand the physical origin of the unexpected formation of metallic Ti instead of TiB_2 as a result of the reaction of TiF_3 and MgB_2, we first theoretically assess the thermodynamic competition between the following possible reactions:

Reaction 1: $TiF_3 + 3/2\ MgB_2 \leftrightarrow Ti + 3/2\ MgF_2 + 3B$ (1)

Reaction 2: $TiF_3 + 3/2\ MgB_2 \leftrightarrow TiB_2 + 3/2\ MgF_2 + B$ (2)

The standard reaction enthalpies (ΔH_{rxn}) are -113 kJ/mole and -392 kJ/mole for Reactions 1 and 2, respectively, based on the NIST-JANAF thermochemical database [39]. As expected from the discussion above, Reaction 2 is far more exothermic and should be favored over Reaction 1 at any reasonable temperature, even after accounting for entropic contributions. For example, the associated configurational entropy changes (ΔS_{rxn}) for the two reactions are calculated as $31.5\ J/(K \cdot mole)$ and $17.4\ J/(K \cdot mole)$, respectively (see the SI for the calculation details)—a difference that is far too low to overcome the enthalpic preference. This confirms that the reaction preference must be kinetically driven.

Given that Reactions 1 and 2 are solid-state reactions, there are two possible kinetic limitations that could account for the observations—namely, diffusion and nucleation. Examining diffusion first, we note that Reaction 2 requires more species to diffuse than does Reaction 1. In both reactions, F atoms and/or Mg atoms must migrate across an interface between MgB_2 and TiF_3 in order to form MgF_2. However, in the case of Reaction 2, Ti and/or B atoms must also migrate across this interface in order to form TiB_2. This need for additional diffusion events likely incurs an associated kinetic penalty, favoring Reaction 1 in agreement with observations.

Next, we consider the phase nucleation kinetics associated with the two reactions. Within classical nucleation theory [40], the critical nucleation barrier (ΔG^*) of product phases can be derived as $4B^3/(27A^2)$, where A represents the driving force for nucleation, and B represents the energy penalty term associated with creating new interfaces during the reactions. The thermodynamic driving force A was derived from the reaction free energy ($\Delta H_{rxn} - T \cdot \Delta S_{rxn}$) as discussed above. The interfacial energy penalty term B was estimated by following an approach demonstrated in our previous work [44], in which surface energy contributions (σ) of the constituent phases are weighted within an assumed generic microstructure model (Figure S2 in the SI). Within this formalism, a weighting parameter (g) acts as the single unknown in the calculation of each interfacial energy term.

We systematically varied the parameter g for the distinct phase boundaries (γ_{TiF_3/TiB_2} and $\gamma_{TiB_2/[MgF_2,B]}$) in order to determine whether conditions exist for which nucleation of Reaction 1 becomes kinetically preferred (see SI for further details). The temperature-dependent nucleation barriers (ΔG^*) for product phases for Reactions 1 and 2, as derived using different assumed values of g that lie within reasonable ranges, are shown in Figure 10. Here, we have plotted our results in terms of the ratio $R = \Delta G_1^*/\Delta G_2^*$, where $R > 1$ indicates that Reaction 2 is preferred, while $R < 1$ indicates Reaction 1 is preferred. Our results confirm that there exist regimes (blue shaded regions in Fig. 10(a) and 10(b)) for which Reaction 1 becomes preferred over Reaction 2 due to nucleation kinetics. Although the exact interfacial energies cannot be determined for our [MgB_2 + 4.46 % TiF_3] system, this analysis proves that the thermodynamic preference for Reaction 2 can be superseded under physically reasonable ranges of g ($g \geq 0.35$ for the TiF_3/TiB_2 interface or $g \geq 0.42$ for the $TiB_2/[MgF_2, B]$ interface, based on the analysis in Figure 10). In summary, we propose that either diffusion or nucleation kinetic limitations may be invoked to explain the experimental observation of Reaction 1 over Reaction 2.

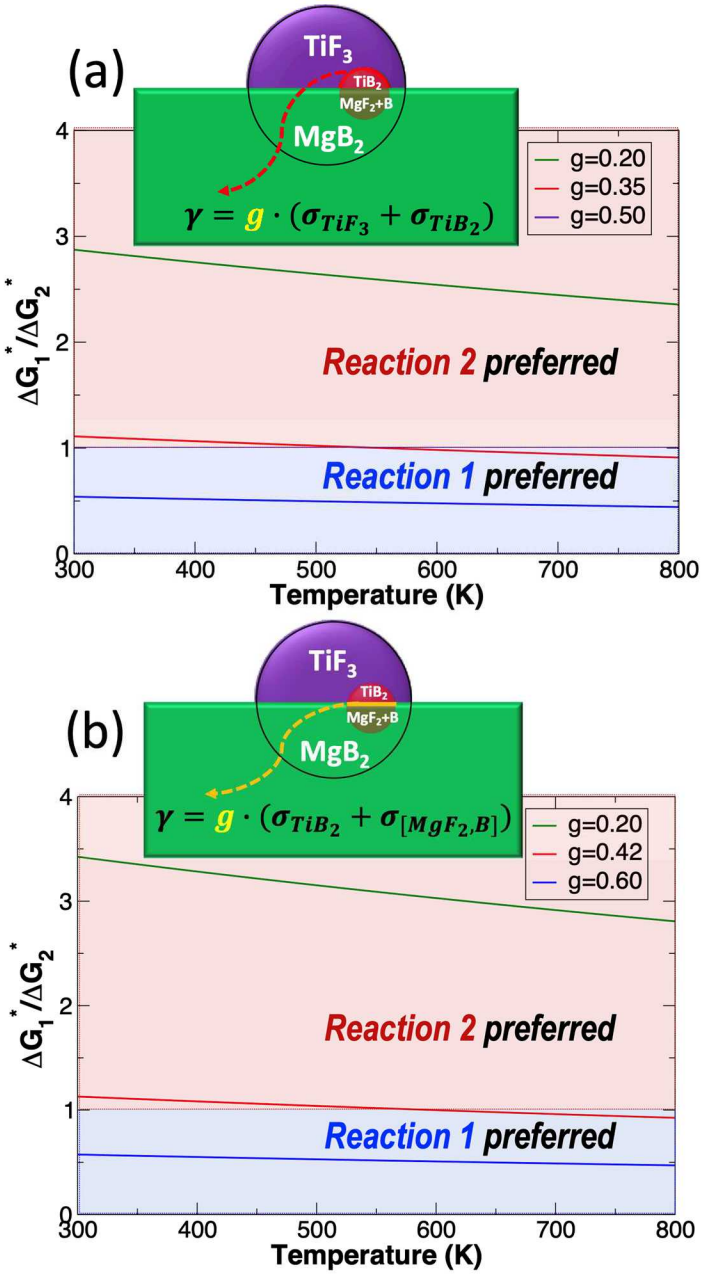

Figure 10: Computed ratio ($\Delta G_1^*/\Delta G_2^*$) of nucleation barriers for the products of Reaction 1 versus those of Reaction 2 as a function of temperature for different values of the interfacial energy parameter (g). Results from varying g for the TiF_3/TiB_2 interface and the $TiB_2/[MgF_2, B]$ interface independently are shown in (a) and (b), respectively; in both cases, all other interfacial energies are held at $g = 0.1$.

To characterize the nucleation kinetics preference, we computed R $(= \Delta G_1^*/\Delta G_2^*)$, where $R > 1$ indicates that Reaction 2 is preferred, while $R < 1$ indicating preferred Reaction 1. Figure 10 shows the computed R as a function of temperature for three selected cases of the distinct interfacial energies within the reasonable ranges. Our results indicate that there exist regimes (see blue regimes in Fig. 10(a) and 10(b), where Reaction 1 is preferred over Reaction 2, forming the metallic Ti experimentally observed in our XAS characterization. Although we are unable to specifically identify such physical conditions of interfaces existing in the [MgB_2 + 4.46 % TiF_3] system, we emphasize that Reaction 1 can preferentially occur in spite of its relatively smaller thermodynamic driving force than Reaction 2 under physically reasonable conditions in terms of the interfacial energy factor (*e.g.*, $g \geq 0.35$ for TiF_3/TiB_2 interface or $g \geq 0.42$ for $TiB_2/[MgF_2, B]$ interface). Summarizing these theoretical considerations of both the diffusion and nucleation kinetic limitations of Reaction 2, we claim that the experimentally observed Reaction 1 is kinetically preferred.

Hydrogenation and H-D Exchange Measurements

Sieverts hydrogenation measurements were conducted for commercial MgB_2, MgB_2 ball-milled for 1 hour, MgB_2 ball-milled for 2 hours, [MgB_2 + 4.88 % Fe], [MgB_2 + 4.97 % Pd] and [MgB_2 + 4.46 % TiF_3]. The results for hydrogen uptake at hydrogen pressures ranging from 130-140 bar and temperatures from 362-377 °C are shown in Figure 11.

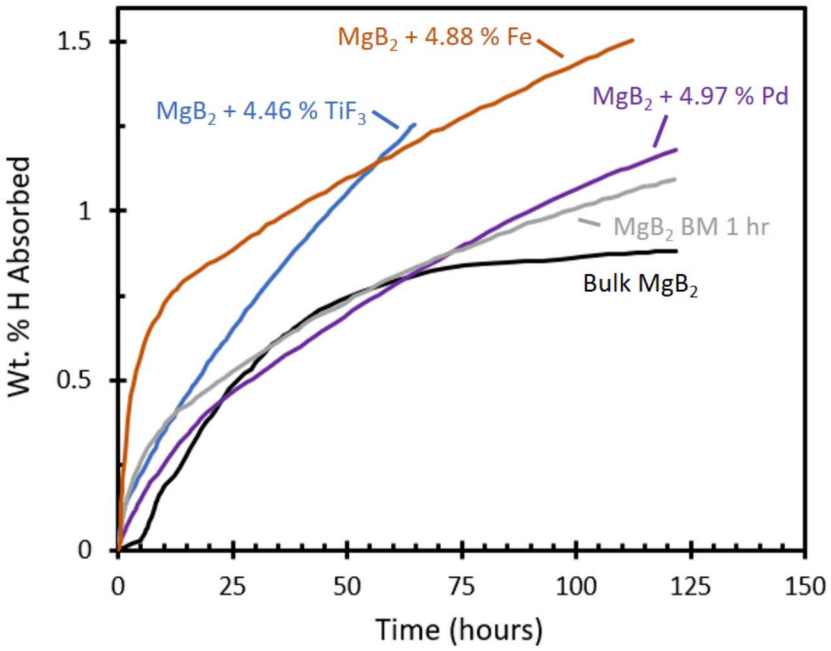

Figure 11: Hydrogen uptake measured as a function of time. The sample temperatures and nominal applied hydrogen pressures were: MgB_2 (364.0 °C, 130 bar), MgB_2 ball milled for 1 hour (364.0 °C, 141 bar), [MgB_2 + 4.88 % Fe] (365.1 °C, 135 bar), [MgB_2 + 4.97 % Pd] (342.7 °C, 122 bar) and [MgB_2 + 4.46% TiF_3] (346.7 °C, 141 bar). The lines are smooth curves through the experimental data.

The data for MgB_2 without additives are generally consistent with prior work [13], where over the course of 100 hours, only ~ 0.8 weight percent hydrogen has been added to the sample. This is a significant amount of hydrogenation, corresponding to a H/MgB_2 mole ratio of 0.4. However, since full conversion of MgB_2 to $Mg(BH_4)_2$ would correspond to 14.9 weight percent of hydrogen added, the level of hydrogenation seen in Figure 11 is far below the hydrogenation potential of MgB_2 and what is needed for practical use of this material for vehicular hydrogen storage. Prior work [13] assigned the initial hydrogenation to the formation of $Mg(BH_4)_2$ from MgB_2 without expression of persistent intermediates. Subsequent theoretical work [45] has recently shown this direct hydrogenation to $Mg(BH_4)_2$ is favored thermodynamically for the pressures and temperature of Figure 11.

As can be seen from Figure 11, the MgB_2 hydrogenation rates for the MgB_2 ball-milled for 1 hour, [MgB_2 + 4.88 % Fe], [MgB_2 + 4.97 % Pd] and [MgB_2 + 4.46 % TiF_3] are somewhat higher than for commercial (as received) MgB_2, but the improvement is very modest, about a factor of two at most, depending on the exposure time and sample. In addition, the amount of hydrogen added remains very modest, ~ 1 weight percent hydrogen. Thus, there is not a significant improvement in the rate of hydrogenation of MgB_2, despite the addition of metals (Pd, Fe and Ti) known to dissociate H-H bonds even at room temperature. Since a modest (but smaller) improvement is also seen for ball-milled MgB_2 without additives, it is difficult to determine whether the relatively modest uptake improvements seen in the additive samples (which were also made by ball milling) is attributable to a functioning of the metal additive itself or else to improvements caused by the creation of reactive defects in the MgB_2 host from ball milling, although we suspect both causes of modest improvement are present.

One could attempt to assign the lack of significant improvement in the MgB_2 hydrogenation rate with additives to a deactivation of the additive by oxidation, or some other form of additive contamination. However, our extensive characterizations discussed already, and presented in detail in the SI, show that the Pd, Fe and Ti additives exist as metals in the MgB_2 matrix. There is no evidence for pathological oxidation which would inactivate the H-H bond breaking ability of these additives, or of chemical reaction to a boride which also might inactivate the additives. Furthermore, there is no evidence for oxidation of the MgB_2 itself to MgO or B-O species which would inhibit the rate of hydrogenation. Rather, the characterization data, combined with the Sieverts data of Figure 11, indicate that the metals introduced are in fact clean and capable of H-H bond breaking in the material. Assuming this is the case, we can reasonably conclude from the lack of substantial H_2 uptake enhancement that H-H bond activation cannot be rate limiting for MgB_2 hydrogenation.

To confirm the H-H bond breaking activity of the materials, and to directly measure the rate of H-H bond breaking that is occurring, we conducted H-D exchange studies of these materials. The basic idea of the experiment is to establish a pressure (typically of order 10 Torr) of H_2 and D_2 over the sample and measure the rate of HD produced by the reaction sequence: $H_2(g) + D_2(g) \rightarrow 2HD(g)$. This reaction does not occur in the gas phase and requires a material that can dissociate H-H and D-D bonds. If the sample can dissociate H-H and D-D bonds, then H_{ads} and D_{ads} atoms are produced on the surface. If the H_{ads} and D_{ads} atoms can diffuse across the surface and find each other, they will form HD_{ads} and then desorb into the gas-phase as HD(g) molecules via the so-called Langmuir-Hinshelwood mechanism [46]. Alternatively, it is possible for H-D exchange to occur initially by the formation of H_{ads} and D_{ads}, followed by reaction of H_{ads} with $D_2(g)$ in the gas-phase (to form D_{ads} and HD(g)) and reaction of D_{ads} with $H_2(g)$ (to form H_{ads} and HD(g)). Such a mechanism is called the Eley-Rideal mechanism of exchange [46]. This alternative mechanism does not require surface diffusion for the HD exchange to occur. The SI gives an extensive discussion and analysis from both experiment and theory of these two mechanisms for producing HD. The conclusion of this analysis is that both the Langmuir-Hinshelwood and Eley-Rideal mechanisms should be operative on MgB_2, with the Eley-Rideal mechanism likely being rate determining for the formation of HD.

Regardless of the mechanism for exchange, the H-D exchange reaction rate can be quantified by comparing the reaction quotient $Q(HD) = [HD]^2 / ([H_2]x[D_2])$ to the expected value at dynamic chemical equilibrium, where the brackets indicate partial pressures of the gas species. Under chemical equilibrium at 22 °C, $Q(HD) = K(HD) = 4.2$, decreasing slightly as temperature increases [47].

Figure 12 displays the results of the HD exchange measurements, plotting the reaction quotient Q versus time for the pressures indicated at 200 °C for the samples examined in this study. For context, we also show results for Fe powder, which is well known to efficiently dissociate hydrogen. The data are plotted on a logarithmic Q scale for Figure 12(a) and on a linear Q scale for Figure 12(b). Figure 12(a) shows that H-H bond breaking is slowest for the bulk MgB_2 material, establishing equilibrium much more slowly than the other samples. It takes about 4 hours for bulk MgB_2 to reach Q = 1.0 at 200 ºC. The [MgB_2 + 4.88 % Fe], [MgB_2 + 4.97 % Pd] and [MgB_2 + 4.46 % TiF_3] samples show dramatically improved rates of H-H and D-D bond breaking, as one would expect for samples with metal additives. For the ball milled MgB_2 samples and the [MgB_2 + 4.88 % Fe], [MgB_2 + 4.97 % Pd] samples, the H-H bond breaking is very fast, and the reaction quotient Q approaches its value for dynamic equilibrium within 15 minutes at T = 200 ºC. The somewhat slower rate observed for the [MgB_2 + 4.46 % TiF_3] sample is a consequence of the weight used for this sample. The H-D exchange was generally so fast that we decided to use only 11 mg of sample for [MgB_2 + 4.46 % TiF_3] (as opposed to the ~ 300 – 400 mg for the other additive samples), to slow the rate of HD exchange in order to better characterize the HD exchange kinetics for this sample.

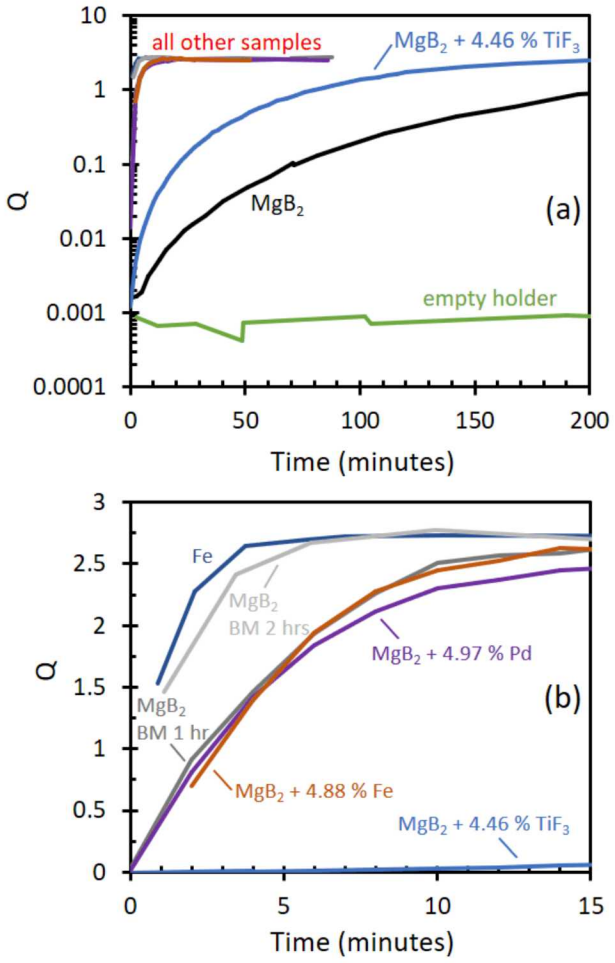

Figure 12: (a) The reaction quotient Q(HD) = $[HD]^2$ / ($[H_2]$x$[D_2]$) plotted on a log scale versus time (hours) for Fe powder, bulk MgB_2, MgB_2 ball milled for 1 hour, MgB_2 ball milled for 2 hours, [MgB_2 + 4.88 % Fe], [MgB_2 + 4.97 % Pd] and [MgB_2 + 4.46 % TiF_3]. The nominal H_2 and D_2 pressures were ~ 6 Torr each. The sample temperature is 200 ºC for all samples; (b) same as (a) only with a linear scaling for the ordinate scale, more clearly showing the results for the Fe powder bulk MgB_2, MgB_2 ball milled for 1 hour, MgB_2 ball milled for 2 hours, [MgB_2 + 4.88 % Fe], [MgB_2 + 4.97 % Pd] and [MgB_2 + 4.46 % TiF_3] samples. The weights of the samples used are given in the Supporting Information.

It is interesting that the MgB_2 samples that had been ball-milled for either 1 or 2 hours without additives also show substantial improvement in hydrogen and deuterium bond dissociation beyond that seen for the commercial bulk MgB_2 powder. The rate of HD exchange at 200 ºC in Figure 12 increases in the order: bulk MgB_2 << MgB_2 ball milled for 1 hour < MgB_2 ball milled for 2 hours. This improvement is attributed to the creation of defects via ball-milling that promote H-H bond dissociation, as well as to an increase in the surface area. Therefore, the H-H bond dissociation occurring in the [MgB_2 + 4.88 % Fe], [MgB_2 + 4.97 % Pd] and [MgB_2 + 4.46 % TiF_3] materials has two contributions: H-H bond breaking at the metallic additive sites, as

well as H-H bond breaking at MgB_2 defect sites produced by ball milling. These contributions from both the additive metal itself and reactive defects in the ball-milled MgB_2 host were discussed analogously for the Sieverts hydrogen uptake measurements of Figure 11.

The H-D exchange experiments in Figure 12 were conducted at 200 °C because early scoping studies indicated that sufficient HD formation occurred on these samples at this temperature. Thus, significant HD production (and therefore H-H bond breaking) occurs ~ 170 °C below the temperatures used for the Sieverts MgB_2 hydrogenation studies shown in Figure 11. The kinetics of HD production increase with temperature, as shown by the H-D exchange results in Figure 13 for [MgB_2 + 4.46 % TiF_3]. Thus, the kinetics of H-H and D-D bond breaking would be even faster than depicted in Figures 12 and 13 if the measurements had been performed at the ~ 360 ºC temperatures used for Sieverts hydrogenation.

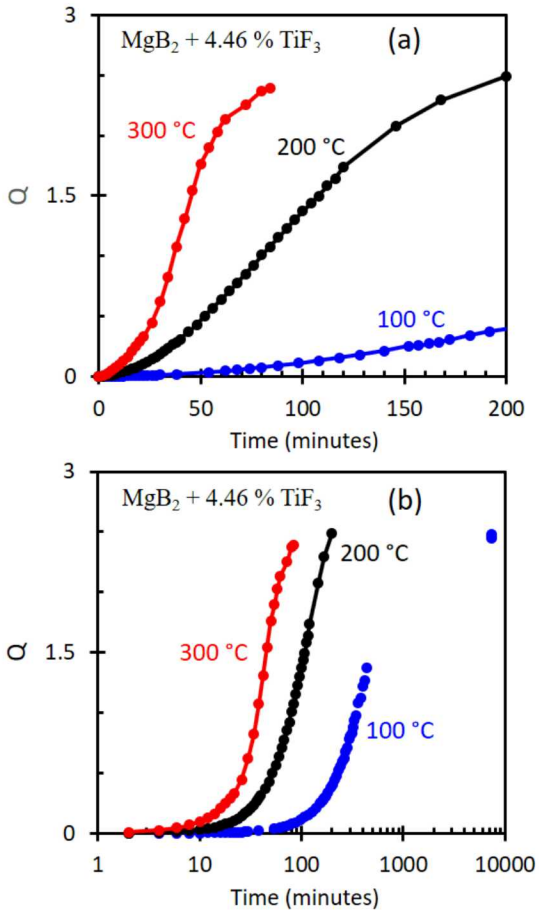

Figure 13: The reaction quotient Q(HD) = $[HD]^2$ /([H_2]x[D_2]) plotted versus time for H-D exchange measurements for 11 mg of [MgB_2 + 4.46 % TiF_3]. (a) results plotted on linear ordinate and abscissa scales at 100 ºC, 200 ºC and 300 ºC for shorter times; (b) results plotted on a logarithmic scale for longer times. The lines through the data connect the points for the 200 °C and 300 ºC results. The nominal H_2 and D_2 pressures are ~ 6 Torr each.

The desorption of the adsorbed HD molecules occurs well below the ~ 300 °C required for $Mg(BH_4)_2$ to release hydrogen. Thus, the atoms deposited on the MgB_2 are not forming hydrogenation products. Since the HD is detected as a desorbed product at T = 200 °C, the H and D atoms must reside in some chemisorbed state that stops short of chemical reaction to form $Mg(BH_4)_2$. The conditions of the HD exchange measurement are much milder than those of the hydrogenation experiments in Figure 11, in terms of temperature (200 °C compared to the 360 °C hydrogenation temperature), pressure (10 Torr compared to the 130-bar hydrogenation pressure) and exposure time (~ 1 hour instead of ~ 100 hours). These conditions conspire to prevent the formation of hydrogenation products such as $Mg(BH_4)_2$ in the HD exchange experiments of Figures 12 and 13.

Figure 12 shows that after ~ 100 minutes, extensive H-H bond breaking has taken place, surface diffusion is active, and the systems are approaching HD exchange equilibrium. In fact, our Arrhenius kinetic analysis [13] of the HD exchange experiments for [MgB_2 + 4.46 % TiF_3] at different temperatures (in Figure 12) identifies that the associated activation energy is within the range of 0.15 ~ 0.3 eV (see Figure S34 in the SI). Notably, this value is quite low—similar to the predicted H diffusion barrier on a clean MgB_2 surface [48], which is consistent with expectations from a Langmuir-Hinshelwood HD exchange mechanism. Nevertheless, the MgB_2 material still requires 100 hours to hydrogenate only partially to 0.8 weight percent hydrogen, as shown in Figure 11. Moreover, our prior work [13] on the mechanism of the initial MgB_2 hydrogenation determined that the activation barrier during hydrogenation varies but never falls below ~0.5 eV—much larger than our observed HD exchange barrier. This confirms that H_2 dissociation kinetics are not meaningfully controlling the MgB_2 hydrogenation reaction kinetics in this regime.

It is worth pointing out that in our prior work [13], the 0.5 eV barrier was associated with an intermediate “diffusive adsorption” step in which adsorbed hydrogen atoms diffuse along the surfaces to reactive sites to form $Mg(BH_4)_2$. If we assume that the HD exchange rate on MgB_2 is determined by the rate of H/D surface diffusion (within the Langmuir-Hinshelwood HD mechanism), we may also conclude that surface diffusion cannot be limiting the initial MgB_2 hydrogenation rate. A full discussion of the nature of the H atom surface diffusion and the mechanism of H-D exchange is given in the SI.

Having determined that H_2 dissociation does not limit the rate of MgB_2 hydrogenation, we can consider alternative possibilities. One possibility is that it is slow bulk diffusion of H in MgB_2 that limits hydrogenation. Another possibility is that it is the intrinsic stability of the B-B extended hexagonal ring structure in MgB_2 that hinders the hydrogenation of this material. If this latter case is true, then bulk MgB_2, MgB_2 ball milled for 2 hours, [MgB_2 + 4.88 % Fe], [MgB_2 + 4.97 % Pd] and [MgB_2 + 4.46 % TiF_3] are not rapidly hydrogenating under our test conditions because their B-B ring structure persists, even upon ball milling and additive addition. A check on this supposition is to directly observe the B-B ring structure in these materials and

see if they are intact. Figures 14(a) and 14(b) presents B K-edge XAS spectra collected in the TFY and TEY modes of detection, respectively, for the materials investigated in this study.

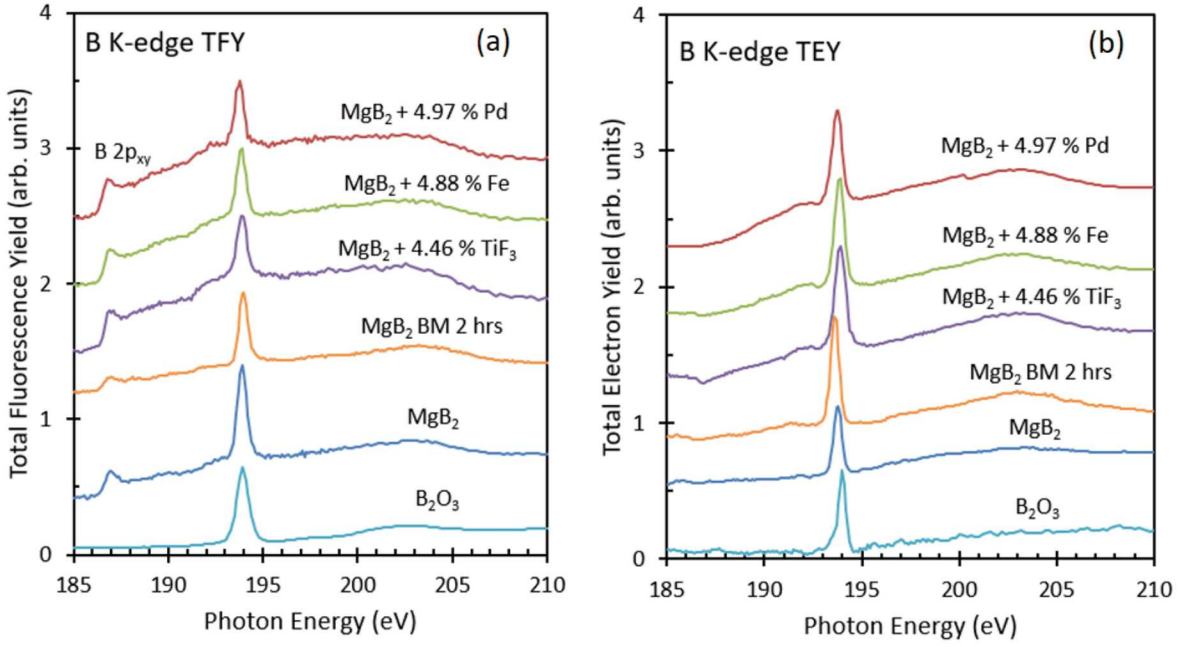

Figure 14: B K-edge x-ray absorption data collected in the (a) TFY and (b) TEY modes for bulk MgB_2, MgB_2 ball-milled for 2 hours, [MgB_2 + 4.46 % TiF_3], [MgB_2 + 4.88 % Fe] and [MgB_2 + 4.97 % Pd]. XAS spectra for B_2O_3 standard powder are also shown for comparison.

The depth sensitivities of the B K-edge TFY and TEY are estimated to be ~ 136 nm and ~4 nm, respectively (see the SI). The small XAS feature in Figure 14(a) at ~ 187 eV photon energy corresponds to photon absorption from the B K shell to the unoccupied B $2p_{xy}$ state just above the Fermi level. This feature is known to originate [13] from the extended B-B ring structure in MgB_2 and does not appear in materials where the B-B ring is absent, for example in B_2O_3.

Figure 14(a) shows that for the MgB_2 sample ball-milled for 2 hours, the B-B ring is still intact, although the unoccupied $2p_{xy}$ feature is diminished slightly compared to that observed from the bulk commercial material. In addition, the three additive samples [MgB_2 + 4.46 % TiF_3], [MgB_2 + 4.88 % Fe] and [MgB_2 + 4.97 % Pd] also show a prominent B $2p_{xy}$ absorption peak, revealing the B-B ring feature is still intact for these samples as well. These XAS results support our supposition that MgB_2 materials with the B-B ring intact are slow to hydrogenate.

Figure 14(b) shows that on the very shallow ~ 4 nm depth scale of the B K-edge TEY measurement, the B $2p_{xy}$ feature is absent in these spectra. This indicates that near the surface the B-B ring is disrupted, perhaps by the existence of the surface, or by surface oxidation of MgB_2, or both. However, it is interesting to note that the TEY spectra for bulk MgB_2, ball-

milled MgB_2, [MgB_2 + 4.46 % TiF_3], [MgB_2 + 4.88 % Fe] and [MgB_2 + 4.97 % Pd] are not identical to B_2O_3. For example, these TEY spectra show spectral intensity just below the intense π^* resonance at 194 eV, spectral intensity that is absent in the B_2O_3 spectrum. This suggests that it is likely a combination of both oxidation and disruption of the normal B-B ring network at the surface conspire to disrupt the B $2p_{xy}$ feature in the B K-edge TEY spectra of Figure 14(b). If our supposition is true that B-B ring disruption is required for faster hydrogenation, then it is at these surface and near-surface sites where the initial hydrogenation of MgB_2 to $Mg(BH_4)_2$ might begin.

Conclusions

We have reported an investigation of potential kinetic limitations to the rate of hydrogenation of MgB_2, both for ball-milled MgB_2 and for MgB_2 ball-milled together with additives. The metals Pd, Fe and Ti, known to activate H-H bond dissociation, were introduced into MgB_2 by ball milling. Pd and Fe are directly introduced as crystalline metals, whereas Ti metal was introduced via the reaction between TiF_3 and MgB_2 to form Ti metal, elemental B and MgF_2. Extensive structural and chemical characterization tests using XRD, FTIR, XAS and TEM showed that the additives persist as metals in the MgB_2 solid, free from significant oxidation of the additive itself (e.g. TiO_2, Fe_2O_3, PdO) as well oxidation of the MgB_2 material (e.g. no MgO, B_2O_3). TEM data shows that the Pd in the MgB_2 material consists of ~ 2 – 25 nm diameter metal particles with a d-spacing essentially the same as bulk Pd. The Fe additive decorates the MgB_2 particles as small particles with sizes ranging from ~ 11 – 34 nm diameter whose d-spacing is identical to the original starting Fe powder. In contrast to Fe and Pd, TiF_3 reacts with MgB_2 to form Ti metal, elemental B and MgF_2. TEM data show that the Ti and the F are smeared out within the MgB_2 base solid but remain proximate to each other.

Sieverts-acquired MgB_2 hydrogenation rates for [MgB_2 + 4.88 % Fe], [MgB_2 + 4.97 % Pd] and [MgB_2 + 4.46 % TiF_3] are higher than for commercial MgB_2, but the improvement is very modest, about a factor of two at most. The Sieverts data, combined with the extensive characterization data, show that the metals introduced are in fact promoting H-H bond breaking in the material, but that promotion does not dramatically improve the MgB_2 hydrogenation rate because H-H bond breaking is not rate limiting for the hydrogenation.

H-D exchange studies of the samples confirm H-H bond breaking and show that H-H bond breaking is slowest for the bulk MgB_2 material, taking about 4 hours to approach equilibrium. For the ball-milled and Fe, Pd and Ti modified MgB_2 samples, H-H bond breaking is very fast, reaching equilibrium in about 20 minutes. The MgB_2 samples that had been ball-milled for 1 - 2 hours without additives also shows substantial improvement in hydrogen and deuterium bond dissociation beyond that seen for the commercial MgB_2 powder, which is attributed to increased surface area and H-H bond-breaking defects created by ball-milling.

This work shows that H-H bond dissociation is not limiting the rate of hydrogenation of MgB_2. A second conclusion is that surface diffusion cannot be limiting the MgB_2 hydrogenation rate because surface diffusion, a likely mechanistic step for HD generation, occurs very rapidly. It may be that the intrinsic stability of the B-B extended hexagonal ring structure in MgB_2 hinders the hydrogenation kinetics. This supposition was supported by B K-edge TFY XAS measurements of the materials, which showed the persistence of the B-B ring structure in these slow-to-hydrogenate materials.

The results indicate that additives chosen to promote H-H bond breaking will be ineffective in accelerating MgB_2 hydrogenation. Although this has been shown here to be true for mesoscale particles of order 100 nm, we suspect it will likely be true for nanoscale MgB_2 particles as well, because the average crystallite size of the MgB_2 samples in our study was found to be ~ 8 nm. Thus, the MgB_2 particles in this study were composed of fused smaller crystallites of nanoscale dimension. Alternatively, it may be that additives that can disrupt the B-B ring network in MgB_2, without penalizing the gravimetric capacity too much, will have greater chance of improving the hydrogenation kinetics of MgB_2. An assessment of this approach is in progress.

It is also possible that other limitations exist that inhibit the hydrogenation of MgB_2 to $Mg(BH_4)_2$. Recently, Vajo et al. have shown [49] that electrolytes, in the form of $LiBH_4/KBH_4$ and LiI/KI/CsI eutectics, can significantly improve the hydrogenation of MgB_2 to $Mg(BH_4)_2$. Although the mechanism of the improvement has not been investigated in detail, it is speculated that the electrolyte improves the dissolution of product $Mg(BH_4)_2$ as it is formed, exposing fresh MgB_2 surface for reaction. The enhancement in MgB_2 hydrogenation kinetics supports the conclusion presented here, that it is not the H-H bond breaking or surface diffusion of H atoms that limits the MgB_2 hydrogenation kinetics. Rather, some other kinetic limitation is operative.

Acknowledgements

The authors acknowledge financial support through the Hydrogen Storage Materials Advanced Research Consortium (HyMARC) of the U.S. Department of Energy (DOE), Office of Energy Efficiency and Renewable Energy, Fuel Cell Technologies Office under Contracts DE-AC52-07NA27344 and DE-AC04-94AL85000. Part of the work was performed under the auspices of the DOE by Lawrence Livermore National Laboratory under Contract DE-AC52-07NA27344. Sandia National Laboratories is a multi-mission laboratory managed by National Technology and Engineering Solutions of Sandia, LLC, a wholly owned subsidiary of Honeywell International Inc., for the DOE's National Nuclear Security Administration under contract DE-NA0003525. Portions of this research were performed on BLs 6.3.1.2 and 8.0.1.1 at the Advanced Light Source, Lawrence Berkeley National Laboratory, which is supported by the Director, Office of Science, Office of Basic Energy Sciences, of the U.S. DOE under Contract DE-AC02–05CH11231. Portions of the research were also performed at the Canadian Light

Source (CLS) on the REIXS beamline BL10ID-2, which is supported by the Canada Foundation for Innovation, Natural Sciences and Engineering Research Council of Canada, the University of Saskatchewan, the Government of Saskatchewan, Western Economic Diversification Canada, the National Research Council Canada, and the Canadian Institutes of Health Research**.** Additional computing resources were provided under the LLNL Institutional Computing Grand Challenge program. Thanks are extended to David Prendergast of Lawrence Berkeley National Lab for helpful conversations, to U.S. Borax, Inc. for providing standard samples of $K_2B_4O_7 \cdot 4H_2O$ and $NaBO_2 \cdot 2\ H_2O$ and to Samantha Lawrence of Los Alamos National Laboratory for no good reason.

References:

1. L. Klebanoff, J. Keller, M. Fronk and P. Scott, *"Hydrogen Conversion Technologies and Automotive Applications,"* Chapter 2 in *Hydrogen Storage Technology, Materials and Applications,* Ed. L.E. Klebanoff (Boca Raton: Taylor & Francis; 2012), p. 31.

2. T. Hua, R. Ahluwalia, L. Eudy, G. Singer, B. Jermer, N. Asselin-Miller, S. Wessel, T. Patterson, J. Marcinkoski, *"Status of Hydrogen Fuel Cell Electric Buses Worldwide,"* J. Power Sources **269** (2014) 975-993.

3. L.E. Klebanoff, J.S. Breit, G.S. Roe, T. Damberger, T. Erbel, S. Wingert et al., *"Fuel Cell Mobile Lighting: A Fuel Cell Market Transformation Project,"* Int. J. of Hydrogen Energy **39** (2014) , 12948-12972.

4. A. Mayyas, M. Wei, S.H. Chan and T. Lipman, *"Fuel Cell Forklift Deployment in the USA,"* Chapter 33 in "Fuel Cells: Data, Facts and Figures," Ed. D. Stolten, R.C. Samsun and N. Garland (Wiley, Weinheim, 2016) p. 334.

5. The first hydrogen fuel-cell rail system for commuter use has been introduced: https://phys.org/news/2018-09-germany-world-hydrogen.html

6. L.E. Klebanoff, J.W. Pratt, C.M. Leffers, K.T. Sonerholm, T. Escher, J. Burgard and S. Ghosh, *"Comparison of the Greenhouse Gas and Criteria Pollutant Emissions from the SF-BREEZE High-speed Fuel-cell Ferry with a Diesel Ferry,"* Transportation Research Part D **54** (2017) 250-268.

7. The feasibility of a hydrogen powered ocean going coastal research vessel (the "Zero-V") has recently been studied. A full report can be downloaded at: https://energy.sandia.gov/transportation-energy/hydrogen/market-transformation/maritime-fuel-cells/

8. The California Air Resources Board has recently funded the construction of the "Water-Go-Round" hydrogen fuel cell ferry. Information about the vessel can be found at: https://watergoround.com/

9. The SAE standard J2719 provides a hydrogen fuel quality standard for commercial proton exchange membrane (PEM) fuel-cell vehicles.

10. The U.S. Department of Energy has established technical performance targets for hydrogen storage systems for onboard storage of hydrogen for light-duty fuel-cell vehicles. These targets can be found at: https://www.energy.gov/eere/fuelcells/doe-technical-targets-onboard-hydrogen-storage-light-duty-vehicles

11. J. Graetz, D.J. Wolstenholme, G.P. Pez, L.E. Klebanoff, G.S. McGrady, and A.C. Cooper, *"Development of Off-board Reversible Hydrogen Storage Materials,"* Chapter 8 in "*Hydrogen Storage Technology, Materials and Applications*", Ed. L.E. Klebanoff, (Taylor and Francis, Boca Raton, 2012) p. 239

12. O. Zavorotynska, A. El-Kharbachi, S. Deledda and B.C. Hauback, *"Recent Progress in Magnesium Borohydride $Mg(BH_4)_2$: Fundamentals and Applications for Energy Storage,"* Int. J. Hydrogen Energy **41** (2016) 14387-14403.

13. K.G Ray, L.E. Klebanoff, J.R.I. Lee, V. Stavila, T. W Heo, P.Shea et al. *"Elucidating the Mechanism of MgB_2 Initial Hydrogenation Via a Combined Experimental-Theoretical Study,"* Phys. Chem. Chem. Phys. **19** (2017) 22646-22658.

14. G. Severa, E. Ronnebro and C.M. Jensen, "*Direct Hydrogenation of Magnesium Boride to Magnesium Borohydride: Demonstration of > 11 Weight Percent Reversible Hydrogen Storage,*" Chem. Commun. **46** (2010) 421-423.

15. R.J. Behm, K. Christmann and G. Ertl, *"Adsorption of Hydrogen on Pd(100),"* Surf. Sci. **99** (1980) 320-340.

16. R.J. Behm, V. Penka, G.-G. Cattania, K. Christmann and G. Ertl, *"Evidence for "Subsurface" Hydrogen on Pd(110): An Intermediate Between Chemisorbed and Dissolved Species,"* J. Chem. Phys. **78** (1983) 7486-7490.

17. T. Engel and H. Kuipers, *"A Molecular-beam Investigation of the Scattering, Adsorption and Absorption of H_2 and D_2 From/On/In Pd(111),"* Surf. Sci. **90** (1979) 162-180.

18. W. Moritz, R. Imbihl, R.J. Behm, G. Ertl and T. Matsushima, *"Adsorption Geometry of Hydrogen on Fe(110),"* J. Chem. Phys. **83** (1985) 1959-1968.

19. F. Bozso, G. Ertl, M. Grunze and M. Weiss, *"Chemisorption of Hydrogen on Iron Surfaces,"* Appl. Surf. Sci. **1** (1977) 103-119.

20. J.C. Cavalier and E. Chornet, "Hydrogen-Deuterium Exchange on Iron: Kinetic Anisotropies," Surf. Sci. **60** (1976) 125-146.

21. P.J. Berlowitz and D.W. Goodman, *"Chemisorption of Ultrathin Pd Layers on W(110) and W(100): Adsorption of H_2 and CO,"* Langmuir **4** (1988) 1091-1095.

22. H.G. Wulz and E. Fromm, *"Hydrogen Absorption Rate of Titanium, Lanthanum, Iron, Nickel, Manganese and Palladium Films With and Without Oxygen Precoverage at 300K,"* J. Less Common Metals **118** (1986) 293-301.

23. T.-U. Nahm and R. Gomer, *"The Adsorption of Hydrogen on W(110) and Fe Covered W(110) Surfaces,"* Surf. Sci. **375** (1997) 281-292.

24. P. M. Abanador, A.R.C. Villagracia, N.B. Arboleda Jr., and M.Y. David, *"First Principle Investigation of Atomic Hydrogen Adsorption on Pd-doped MgB_2,"* Philippine Science Letters **6** (2013) 176-181.

25. D. Saha and S. Deng, *"Hydrogen Adsorption on Ordered Mesoporous Carbons Doped with Pd, Pt, Ni and Ru,"* Langmuir **25** (2009) 12550-12560.

26. M. Pozzo and D. Alfe, *"Hydrogen Dissociation and Diffusion on Transition Metal (= Ti, Zr, V, Fe, Ru, Co, Rh, Ni, Pd, Cu, Ag)-doped Mg(0001) Surfaces,"* Int. J. Hydrogen Energy **34** (2009) 1922-1930.

27. S. Kang, L.E. Klebanoff, A.A. Baker, D.F. Cowgill, V. Stavila, J.R.I. Lee, M.H. Nielsen, K.G. Ray, Y.-S. Liu and B.C. Wood, *"Assessing the Reactivity of $TiCl_3$ and TiF_3 With Hydrogen,"* Int. J. Hydrogen Energy **43** (2018) 14507-14519.

28. G. Teeter and J.L. Erskine, *"Surface Relaxation of Ti(0001): Influence of Hydrogen Contamination,"* Phys. Rev. B **61** (2000) 13929-13935.

29. N.B. Arboleda Jr., H. Kasai, K. Nobuhara, W.A. Dino and H. Nakanishi, *"Dissociation and Sticking of H_2 on Mg(0001), Ti(0001) and La(0001) Surfaces,"* J. Phys. Soc. Japan **73** (2004) 745-748.

30. M. Pozzo, D. Alfe, A. Amieiro, S. French and A. Pratt, *"Hydrogen Dissociation and Diffusion on Ni- and Ti-doped Mg(0001) Surfaces,"* J. Chem. Phys. **128** (2008) 094703 1-11.

31. A. Clark, *"Oxides of the Transition Metals as Catalysts*," Industrial and Engineering Chemistry **45** (1953) 1476-1480.

32. D.A. Dowden, N. Mackenzie and B.M.W. Trapnell, *"Hydrogen-Deuterium Exchange on the Oxides of Transition Metals,"* Advances in Catalysis **9** (1957) 65-69.

33. W. Göpel, G. Rocker and R. Feierabend, *"Intrinsic Defects of TiO_2(110): Interaction with Chemisorbed O_2, H_2, CO and CO_2,"* Phys. Rev. B **28** (1983) 3427-3438.

34. H. Hagemann, V. D'Anna, J.-P. Rapin and K. Yvon, *"Deuterium-Hydrogen Exchange in Solid $Mg(BH_4)_2$,"* J. Phys. Chem. C **114** (2010) 10045-10047.

35. A. Borgschulte, A. Züttel, P. Hug, G. Barkhordarian, N. Eigen, M. Dornheim, R. Bormann and A.J. Ramirez-Cuesta, *"Hydrogen-deuterium Exchange Experiments to Probe the Decomposition Reaction of Sodium Alanate,"* Phys. Chem. Chem. Phys. 10 (2008) 4045-4055.

36. W. Lohstroh and M. Fichtner, *"Rate limiting Steps of the Phase Transformations in Ti-doped $NaAlH_4$ Investigated with Isotope Exchange,"* Phys. Rev. B **75** (2007) 184106-1-6.

37. A. Erbil, G.S. Cargill III, R. Frahm, R.F. Boehme, *"Total-electron-yield Current Measurements for Near-surface Extended X-ray Absorption Fine-structure,"* Phys. Rev. B **37** (1988) 2450-2465.

38. J. Jaklevic, J.A. Kirby, M.P. Klein, A.S. Robertson, G.S. Brown, P. Eisenberger, *"Fluorescence Detection of EXAFS - sensitivity enhancement for dilute species and thin-films,"* Solid State Comm. **23** (1977) 679-682.

39. M.W. Chase, *"NIST-JANAF Thermochemical Tables,"* American Institute of Physics for the National Institute of Standards and Technology, Washington, D.C.; Woodbury, N.Y., 1998.

40. D.A. Porter, K.E. Easterling and M. Sherif, M., *"Phase Transformations in Metals and Alloys,"* (Revised Reprint). CRC press: 2009.

41. G. Kresse and J. Furthmüller, *"Efficient Iterative Schemes for ab-initio Total-energy Calculations Using a Plane-wave Basis Set,"* Phys. Rev. B **54** (1996) 11169-11186.

42. A.W. Burton, K. Ong, T. Rea and I. Y. Chan, *"On the Estimation of Average Crystallite Size of Zeolites from the Scherrer Equation: A Critical Evaluation of its Application to Zeolites with One-dimensional Pore Systems,"* Microporous and Mesoporous Materials **117** (2009) 75-90.

43. L. Rao, E. G. Gillan and R.B. Kaner, *"Rapid Synthesis of Transtion-metal Borides by Solid-state Metathesis,"* J. Mater. Res. **10**, (1995) 353-361.

44. B.C. Wood, V. Stavila, N. Poonyayant, T.W. Heo, K.G. Ray, L.E. Klebanoff, T.J. Udovic, J.R.I. Lee, N. Angboonpong, P. Pakawatpanurut, *"Nanointerface-driven Reversible Hydrogen Storage in the Nanoconfined Li-N-H System*" Adv. Mat. Interfaces **4**, (2017) 1600803 1-7.

45. Unpublished results of S. Kang and B.C. Wood, Lawrence Livermore National Laboratory.

46. P.W. Atkins and J.de Paula, *"Physical Chemistry: Thermodynamics, Structure and Change,"* 10th ed. (W.H. Freeman and Company, New York, 2014) p. 956.

47. W.F. Luo, D.F. Cowgill, R.A. Causey, *"Thermodynamic and Kinetic Characterization of Hydrogen-deuterium Exchange in Beta-phase Palladium,"* J. Phys. Chem. B **113** (2009) 12978-12987.

48. Y. Wang, K. Michel, Y. Zhang and C. Wolverton, *"Thermodynamic Stability of Transition Metals on the Mg-terminated MgB_2(0001) Surface and Their Effects on Hydrogen Dissociation and Diffusion,"* Phys. Rev. B **91** (2015) 155431 1-11.

49. J.J. Vajo, H. Tan, C.C. Ahn, D. Addison, S.-J. Hwang, J.L. White, T.C. Wang, V. Stavila and J. Graetz, *"Electrolyte-Assisted Hydrogen Storage Reactions,"* J. Phys. Chem. C **122** (2018) 26845 – 26850.